Radial structure of the constricted positive column: Modeling and experiment

Yu. Golubovskii, D. Kalanov,* and V. Maiorov
Saint Petersburg State University, 7/9 Universitetskaya nab., Saint Petersburg, 199034 Russia
(Received 24 January 2017; revised manuscript received 25 June 2017; published 16 August 2017)

We present a detailed self-consistent model of a positive column in argon glow discharge at moderate pressures and currents. This model describes the discharge transition between diffuse and constricted states. The model includes an extensive set of plasma chemical reactions and equation for inhomogeneous gas heating. The nonequilibrium behavior of an electron distribution function is also considered. One of the main features of the model is an accurate treatment of radiation trapping by solving the Holstein-Biberman equation directly. Influence of the radiation trapping on macroscopic parameters of the constricted positive column is studied. We propose a method for solving a boundary-value problem, including particle and energy balance equations for electrons, ground state atoms, atomic and molecular ions, and excited species. Unlike traditional solution approaches for similar systems, the method provides continuous Z- and S-shaped characteristics of discharge parameters, describing hysteresis in transition between diffuse and constricted discharge regimes. Performed experiments include measurements of volt-ampere characteristics and spectroscopic study of radial density profiles of excited atoms by measuring line emission and absorption, and electrons by measuring bremsstrahlung intensity. The role of resonance radiation trapping in spatial redistribution of $1s$ and $2p$ states of argon is demonstrated. Results of modeling are compared to the experimental data.

DOI: 10.1103/PhysRevE.96.023206

I. INTRODUCTION

Since early studies of a gas discharge, the constriction phenomenon has been a problem of high interest. Many qualitative descriptions were proposed over the years [1–8]. In Refs. [1,2] thoughts on radial dissociation of molecular ions have been proposed. To explain constriction of the glow discharge various explanations were given, which are typical for thermal arc plasmas [3–7]. Those descriptions were based on inhomogeneous gas heating. In Ref. [8] an alternative viewpoint was proposed. That approach was based on a solution of the kinetic equation not considering the gas heating. It was suggested that constriction is caused by a competition between electron-electron and electron-atom collisions, which increase the losses of fast electrons and narrow the ionization sources. Over the last decades various detailed collisional-radiative models with extensive sets of plasma-chemical reactions were developed [9–14]. A summary of previous works on this topic was made in Ref. [15].

Qualitatively the phenomenon of constriction can be described as following. At lower pressures and currents (about 3 Torr, $<$ 10 mA) ionization is proportional to the electron density, charged particles are moved to the tube walls due to the ambipolar diffusion. It results in smooth radial profiles of electron density and ionization sources. With an increase of the pressure and the current (around 5–10 Torr, 10–15 mA), ionization sources start compressing to the axis. Reasons for that compression are the gas heating and the role of Coulomb collisions in the formation of the electron energy distribution function (EEDF). The gas heating causes a radial decrease of the reduced electric field E/N, where N is the neutral gas density. That radial decrease forces a compression of the ionization zone due to the exponential dependence. Coulomb collisions reveal another exponential dependence: ionization rate on the ionization degree. It forces additional strong compression of the column. While the losses of charged particles are determined by its diffusion, one observes an "optical constriction." In this case, the zones of ionization and excitation are narrow, but the current conduction zone is broadened. With the further increase of the pressure and the current ($>$20 Torr, $>$20 mA) the volume recombination starts to dominate. Electrons and ions originated near the axis move towards the wall on a distance, defined by a recombination time. Charged particles recombine outside this area. Above such pressures, when the current reaches the critical value, an abrupt transition to the constricted state happens. Finally, the main reasons for the constriction are related to the abrupt compression of the ionization zone and the volume recombination.

The so-called phenomenon of constriction is observed in short low-current discharges at low pressures, particularly during a transition from the Townsend regime to the glow. A range of problems related to that phenomenon including its evolution dynamics was studied in works [16,17]. In that range of discharge parameters in the near-cathode areas, the presence of space charges and axial inhomogeneity plays a crucial role. Unlike those works, in the present paper and cited literature, a theory of the stationary long positive column is described. That column is assumed to be an axially homogeneous and radially inhomogeneous infinite cylinder. The considered parameter range for pressures and currents is tens and hundreds of Torr and dozens and hundreds of mA, respectively.

By using detailed models, it becomes possible to explore details of the ionization processes, the role of the inhomogeneous gas heating, the ion-molecular plasma composition, etc. Description of the hysteresis in abrupt transition between diffuse and constricted states is an essential problem. This effect was experimentally found in Ref. [18]. The first interpretation of this hysteresis was based on a self-consistent solution of the kinetic equation, balance equations for ions and electrons, and

*kalanoff@gmail.com

an equation for the electric circuit. Quite flexible methods were proposed for the solution of that system. Z-shaped volt-ampere characteristics (VACs), including unstable branches, were obtained theoretically. The abrupt transition was interpreted as a leap between two branches (diffuse and constricted) under constant current due to the ionization instability. Existing numerical models can describe this transition by the overlap of two branches. In the hysteresis area, numerical solution converges either to diffuse or to a constricted branch. To summarize, one may conclude that the theory of constriction is sufficiently complete. However, it should be mentioned that in all those theories particle transport was mainly diffusive. In particular, transport of the resonance atoms for constricted discharges was described using local escape factor approximation introduced by Holstein and Biberman [19–21]. In works of Phelps [22–24] the Holstein-Biberman theory was included in models of a glow discharge.

Different ways to solve the Holstein-Biberman equation more accurately were proposed over the years [25–31]. An efficient method, based on solving the equation directly by plasma volume discretization, was described in Ref. [32]. In constricted discharges, where the electron density is high enough, mixing of excited atoms become intensive, and radiation transport becomes the primary transport mechanism for these particles. In Ref. [33] resonance radiation trapping was studied in a simple model without gas heating and with simplified plasma chemistry.

Current work deals with a new problem which was not discussed earlier: the influence of resonance radiation transport on densities of various excited species and the mechanism of the glow discharge constriction in conditions mentioned above. Detailed self-consistent model of a positive column in argon glow discharge is presented. Measurements of volt-ampere characteristics and radial distributions of electrons and excited atoms are performed.

II. THE BASIC EQUATIONS AND SOLUTION METHODS

A. The kinetic model

In the present work detailed modeling of the argon discharge is performed, including sets of reactions, similar to previous models [10–14]. The main distinctive features of the present model is an accurate treatment of the resonance radiation transport and the possibility to obtain a continuous hysteresis in transition between diffuse and constricted regimes.

The model includes four lower excited atomic states ($2p_6 4s$) and ten $2p_6 4p$ levels ($1s$ and $2p$ in Pashen's notation). Elementary processes with those states include excitation and ionization by electron collisions, intermixing with electrons and radiative transitions between considered groups, as well as resonance transitions to the ground state. In the present model ions of two sorts, atomic and molecular, are taken into account. Mobility of atomic ions under normal conditions ($p = 1$ atm, $T_g = 300$ K) is 1.67 V cm^{-1}s^{-1} and for molecular ions is 1.9 V cm^{-1}s^{-1} [34]. Excimer molecules Ar_2^* are dominantly in the state $Ar_2^*(^3\Sigma_u)$ [35], so only this dimer is considered.

Elementary processes, included in the model, are listed in Table I. Most of the rate constants of processes with electrons are calculated by integration of the cross sections and the electron energy distribution function (EEDF). The EEDF is obtained by solving the Boltzmann equation, and corresponding rates are indicated by "BE" in the table.

B. Balance equations

In the present model, one needs to define balance equations for the following species: n_e, n_i, and n_{2i}, electrons and ions of two sorts, resonance and metastable $1s$ and radiating $2p$ excited states, and a thermal balance equation.

Atomic ions are produced by step ionization ν_{step} and destroyed by conversion to molecular ions Z_{conv}. Three-body

TABLE I. Reactions included in the collisional-radiative model.

Process	Notation	Rate constant (cm^3 s^{-1})	Ref.
Elastic scattering	$Ar + e \rightarrow Ar + e$	BE	[36]
Excitation	$Ar + e \rightarrow Ar^*(1s) + e$	BE	[36]
Excitation	$Ar + e \rightarrow Ar^{**}(2p) + e$	BE	[36]
Intermixing	$Ar^* + e \rightarrow Ar^* + e$	BE	[37,38]
Direct ionization	$Ar + e \rightarrow Ar^+ + 2e$	BE	[36]
Stepwise ionization	$Ar^* + e \rightarrow Ar^+ + 2e$	BE	[36]
Chemoionization	$Ar^* + Ar^* \rightarrow Ar_2^+ + e$	6.4×10^{-10}	[37]
Ion conversion	$Ar^+ + 2Ar \rightarrow Ar_2^+ + Ar$	$2.3 \times 10^{-31}(300/T_g)^{0.67}$ cm^6 s^{-1}	[39]
Dissociative recombination	$Ar_2^+ + e \rightarrow Ar^* + Ar$	$9.1 \times 10^{-7}(300/T_e)^{0.61}$	[40]
Dissociation	$Ar_2^+ + e \rightarrow Ar^+ + Ar + e$	BE	[41]
Excimer formation	$Ar^* + 2Ar \rightarrow Ar_2^* + Ar$	$1.4 \times 10^{-32}(T_g/300)^{0.5}$ cm^6 s^{-1}	[14]
Destruction by e	$Ar_2^*(^3\Sigma_u) + e \rightarrow Ar + e$	5×10^{-8}	[35]
Resonance radiation	$Ar^*(1s_4) \rightarrow Ar + h\nu$	1.2×10^8 s^{-1}	[42]
Resonance radiation	$Ar^*(1s_2) \rightarrow Ar + h\nu$	5.1×10^8 s^{-1}	[42]
Excimer radiation	$Ar_2^*(^3\Sigma_u) \rightarrow 2Ar + h\nu$	3.5×10^5 s^{-1}	[43,44]
Visible radiation	$Ar^{**} \rightarrow Ar^* + h\nu$	A_{ik}, s^{-1}	[42]
Metastable diffusion	$Ar^* \rightarrow$ wall	40 cm^2 s^{-1} Torr^{-1}	[45]

recombination is neglected. Molecular ions are produced by chemo-ionization $Z_{\rm chem}$ and conversion, being destroyed by dissociative recombination with rate α. Ambipolar diffusion is taken into account for both types of ions. The radial electric field in case of ambipolar diffusion is defined as $E_r = -kT_e/e(\nabla n_e/n_e)$. Rates $\nu_{\rm step}$ and α also depend on the electric field and electron density.

The equation for metastable states has the form

$$-\frac{1}{r}\frac{\partial}{\partial r}\left(rD_k\frac{\partial N_k}{\partial r}\right) = n_e W_k - n_e N_k\left(\nu_k^{\rm step} + \sum_i \nu_{ki}\right) + \sum_i N_i(n_e\nu_{ik} + A_{ik}\delta_{i,2p}),$$
$$N_k'(0) = 0, \quad N_k(R) = 0. \tag{1}$$

Here W_k is a direct excitation rate, ν_{ik} is a frequency of mixing transition from a ith to a kth state, and D_k is a metastable diffusion coefficient.

The balance of resonance atoms can be expressed as

$$A_k N_k - A_k\int_{(V)} N_k(r')K(r',r)\,dr = n_e W_k - n_e N_k\left(\nu_k^{\rm step} + \sum_i \nu_{ki}\right) + \sum_i N_i(n_e\nu_{ik} + A_{ik}\delta_{i,2p}), \tag{2}$$

where A_k is the radiative transition probability for the kth resonance state. The integral term describes spatial redistribution of atoms due to the transport of resonance radiation. Balance equations for $2p$ states are defined similarly.

Gas heating should be considered to analyze the radial distributions because it affects the filament radius. Thermal balance equation reads [14]

$$-\frac{1}{r}\frac{\partial}{\partial r}\left\{r\lambda[T_g(r)]\frac{\partial T_g(r)}{\partial r}\right\} = H_{el}(r). \tag{3}$$

Here ρ is a gas density and $\lambda(T_g)$ is thermal conductivity. The term

$$H_{el}(r) = 2\frac{m}{M}\sqrt{\frac{2}{m}}\int_0^\infty u^2 N\sigma_{el}(u)f_0(u,r)\,du \tag{4}$$

describes heating due to elastic collisions, which is the dominant process in noble gases. Dependence $\lambda(T_g)$ in the temperature range < 900 K can be approximated as $\lambda(T_g) = 7.6063\times10^{-6} + 3.776\times10^{-7}T_g$ (W cm^{-1}K^{-1}) [14]. If the gas is heated, then the pressure will increase, and an expression for the ground state atoms will have the form

$$N(r) = \frac{N_0R^2}{2T_g(r)}\left[\int_0^R \frac{r\,dr}{T_g(r)}\right]^{-1}. \tag{5}$$

A solution method for the balance equation system, involving resonance radiation transport, was described in Ref. [32]. The plasma volume is discretized assuming that the resonance atom density is constant within the unit volume. The differential operators are treated using finite differences, and the integral operator in Eq. (2) is reduced to a linear equation system by an integration of the operator kernel over unit volumes. For example, the left-hand side of Eq. (2) becomes $A_{\rm eff}\sum_m a_{mn}N_k(r_n)$.

The limits of the present theory should be discussed. The lower limit for a current is about 5 mA, and the pressure should be higher than 10 Torr. At such conditions, the plasma can be considered as quasineutral, and the electron energy distribution function (EEDF) is local due to elastic and Coulomb collisions. It is assumed that the near-electrode zones are much shorter than the length of a positive column. With an increase of the pressure, current and input power the plasma becomes more thermal, from nonequilibrium state to the LTE in arc discharge through the partial LTE. Such transition is allowed in our theory if supplemented by rates of all reverse plasma-chemical processes. The present model is best suited for conditions under the upper Pupp's border for the pressure and current [46] because constriction and stratification have quite similar causes.

C. Solution algorithm

The first step in the solution of the problem is the determination of the EEDF. Under given discharge conditions ($n_e \sim 10^{10} \to 10^{13}$ cm^{-3}, $n_e/N < 10^{-3}$, $p = 42$ Torr) EEDF can be found by solving the kinetic equation, considering elastic and inelastic electron-atom collisions along with electron-electron interaction. The Boltzmann equation is solved in a local approximation in the same way as in Ref. [33], being nonlinearly dependent on two parameters: reduced electric field E/N and ionization degree n_e/N. Instead of calculation at each step of a global loop, EEDF is calculated once and derived macroscopic quantities are tabulated for the whole assumed range of electron densities and reduced electric fields: excitation, ionization and recombination rates, dissociation rate, electron mobility b_e, and electron temperature T_e. The table ranges were n_e, $(10^8 \to 10^{14})$ cm^{-3}, and E/N, $(0.1 \to 7)$ V cm^2. The scheme of discretization of the kinetic equation was described in detail in Ref. [47]. Macroscopic quantities are obtained by integrating EEDF over the energy.

The second step is the calculation of the radiation transport matrix in the infinite cylindrical geometry. It is computed once before the global loop as described in Ref. [32]. The computational time of this matrix depends on a number of the unit volumes. In the case of 62 radial steps, the matrix was computed for 2 min approximately (using Intel Core i7-3630QM CPU 2.40 GHz). This value provided good agreement with results on denser mesh, so it was taken as optimal. For comparison, the total time of the solution loop can be 40–60 min. Therefore, the radiation transport does not affect the computational cost significantly.

The next step is to solve the system of balance equations. Traditionally, the constriction problem was solved as time-dependent [10–14]. First, the external input parameters were specified (such as the current i, the pressure p, the tube radius R, the gas type and computed plasma-chemical rates). Second, initial values of internal variables were specified (including E, N_e, $N_{\rm exc}$, etc.). Then the time-dependent problem is solved to obtain established self-consistent values of internal variables as functions of the external characteristics. For example, the electric field is obtained as a function of the current. Such a method has difficulties with a solution in the hysteresis area. In

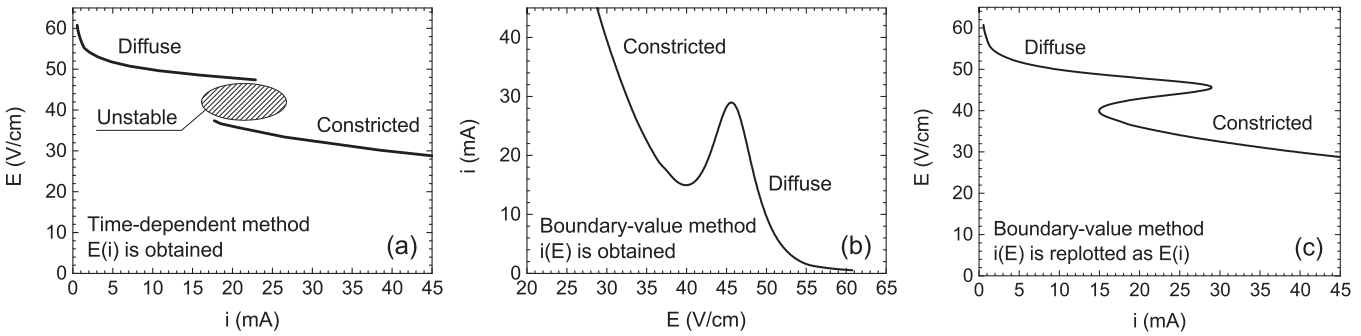

FIG. 1. Example of the field-current characteristic obtainable with different solution approaches. (a) The traditional time-dependent method; (b, c) the stationary boundary-value method.

this unstable zone, the solution converges either to the upper diffuse branch or to the lower constricted branch of the field-current characteristic [Fig. 1(a)].

Another way to solve the problem is to use the stationary boundary-value form. Boundary conditions for the diffusion equations are a zero derivative on the axis and a zero value on the tube wall. The integral Holstein-Biberman equation does not require boundary conditions. External input parameters are p, R and rates of plasma-chemical processes. Also, the electric field E is fixed, and initial values of the densities and initial radial profiles are set. Then for fixed E the axial electron density is varied until the boundary conditions are met. Finally, the discharge current is calculated, and the procedure is repeated for the next value of E. Thus one can obtain the self-consistent continuous characteristics as functions of the electric field [for example, the current-field characteristic, Figs. 1(b) and 1(c)] and the radial density distributions of various plasma species. The solution algorithm is illustrated in Fig. 2. A similar idea was discussed in the frame of a simple ionization balance model [48].

III. EXPERIMENTAL METHODS

The experimental setup is similar to that described in Ref. [49] with some improvements. It is presented in Fig. 3. A vertically oriented cylindrical discharge tube with a radius of 2.3 cm had two electrodes with a distance $d = 50$ cm between them. Vertical orientation was chosen to avoid radial asymmetry due to floating of the discharge. Spectrally pure argon was fed through the vacuum system with liquid-nitrogen cooled traps. A power supply used in this setup could maintain discharge with currents of up to 200 mA. In the present measurements, the gas pressure was 42 Torr, and a DC glow discharge was investigated in a range of currents 5–50 mA.

For spatial absorption measurements, the second tube with an inductively coupled plasma (ICP) discharge filled with 2 Torr argon was placed behind the primary source. A back window of the source tube was uniformly illuminated by using a lens and projected on the entrance slit of a spectral device. A registration system consisted of monochromator Acton SpectraPro 2300i, which can record either with a photodetector PD-438 or with a high-speed camera pco.1200hs. Radial scanning with the photodetector was performed by rotating a plane-parallel plate.

To ensure high enough spatial resolution to measure constricted plasma cord with radius of about 1 mm, the source was placed far away from the main lens. As a result, the image is reduced 17 times in the radial direction and 17^2 times in the longitudinal direction. The entrance slit width was 0.02 mm, and the exit slit before the photomultiplier was 0.04 mm. Optical measurements in constricted plasma, where the radiating cord can be about 1 mm radially, are

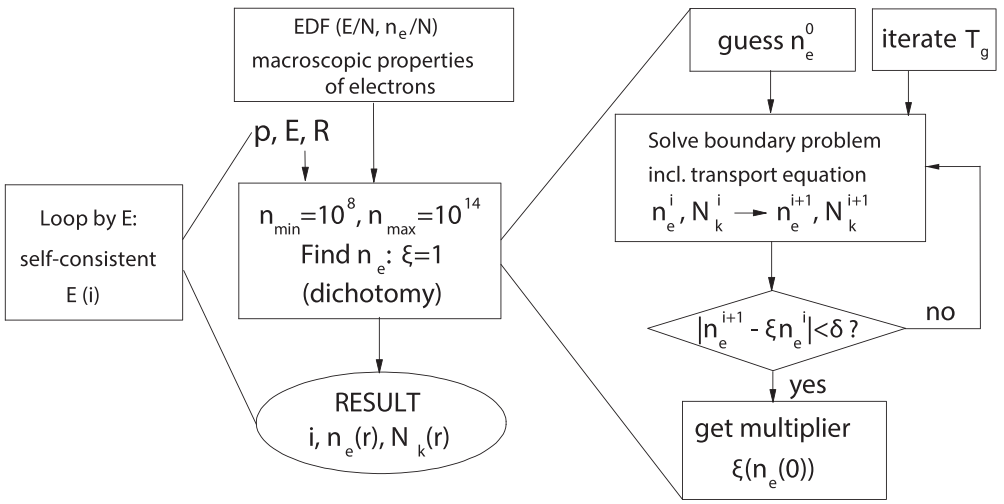

FIG. 2. Scheme of the self-consistent calculation.

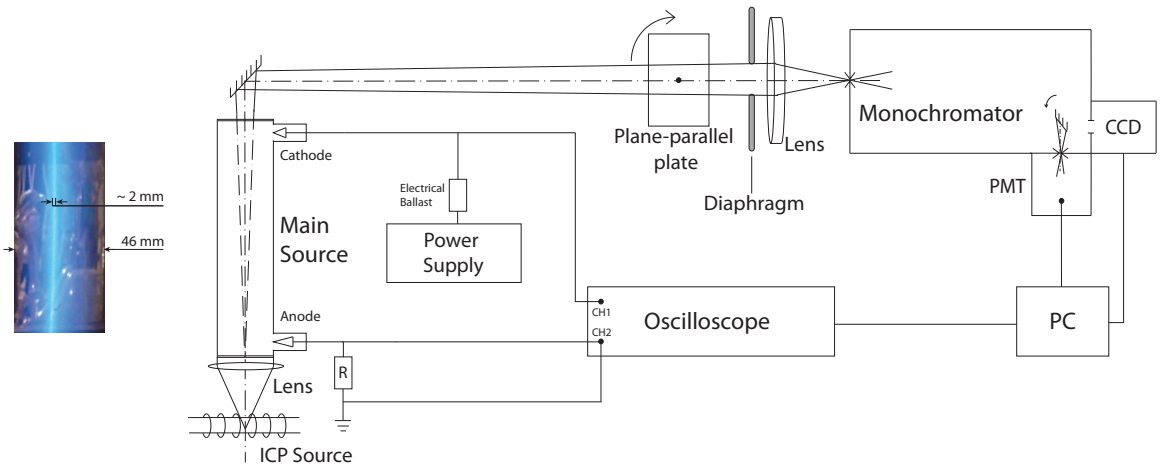

FIG. 3. Scheme of the experimental setup. Fragment of the constricted discharge (on the left).

quite sensitive to the spatial resolution of the setup, and it seems necessary to take into account instrument distortions. Determination of the instrument function of a volumetric source is not a trivial problem. It was measured for the current setup in Ref. [49]. Direct account of the instrument distortions by solving an inverse problem seems inefficient due to large signal-noise ratios in measurements. Since experimental data are compared to results of the simulation, instrument distortions can be taken into account by convolution of the instrument function with a calculated radial intensity profile. This procedure is illustrated by Fig. 4. All theoretical curves, which are compared with the experiment in the "Results and Discussion" section, are already broadened by the instrument function.

Radial density profiles of $1s,2p$ levels of argon were obtained using classical absorption and emission methods. An absorption function was measured:

$$A = \frac{\Phi_2 + \Phi_1 - \Phi_{1+2}}{\Phi_1}. \tag{6}$$

Here Φ_2 is a photon flux from the source tube, Φ_1 is a flux from the transilluminating tube, and Φ_{1+2} is a total signal from both tubes. Radial density profiles of the radiating $2p$ levels are determined by spectral line intensity distribution Φ_2, corrected for reabsorption within the source. Densities of the absorbing $1s$ levels can be determined by solving radiation transport equation supplemented by a boundary condition for the Φ_1 source:

$$\frac{\Phi_\nu(x)}{dx} = I_\nu(x) - k_\nu(x)\Phi_\nu(x), \Phi_{x=0}(r) = \Phi_{1,\nu}. \tag{7}$$

Integration over the coordinate x and the frequency ν leads to

$$\Phi_{1+2}(K_0L) = I_0 L S(K_0L) + \Phi_1 \int_0^\infty \varepsilon_\nu e^{-k_\nu L}\, d\nu. \tag{8}$$

The first term on the right-hand side is the flux Φ_2. Here $S(K_0L)$ is the well-known Ladenburg function [50], which describes a probability of photon escape along the line-of-sight, accounting for the reabsorption; ε_ν, k_ν are emission and absorption line contours, respectively. The second term describes absorption of the flux Φ_1 along the length L. Substituting Eq. (8) into Eq. (6), the absorption function reads

$$A(K_0L) = 1 - \int_0^\infty \varepsilon_\nu e^{-K_\nu L}\, d\nu. \tag{9}$$

The absorption function, determined by measured fluxes, provides information about the absorption coefficient in the line center K_0 and about the densities of absorbing atoms, respectively.

Examples of the spatial profiles of sources $\Phi_1, \Phi_2, \Phi_{1+2}$ for some $2p \rightarrow 1s$ transitions in argon are presented in Fig. 5. These examples clearly illustrate the difference between weakly and highly absorbed transitions [cases (a) and (d) respectively].

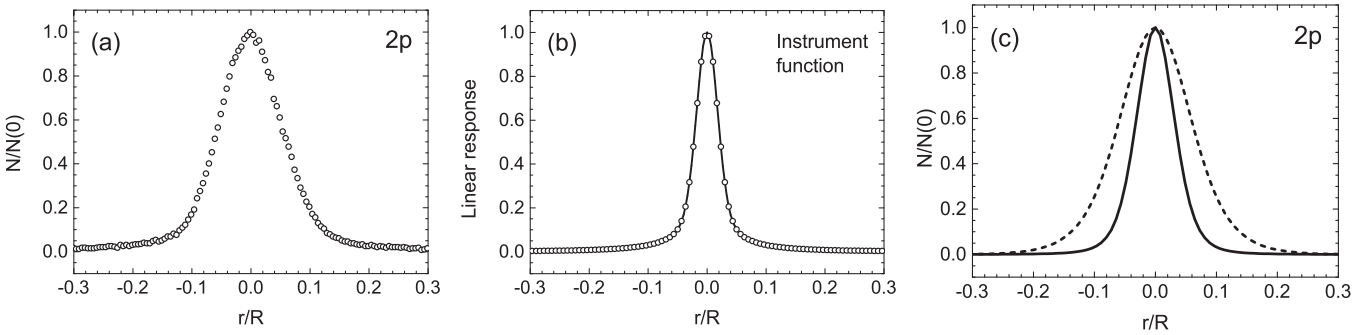

FIG. 4. (a) Measured density profile of the $2p$ state. (b) Instrument function of the experimental setup. (c) Calculated density profile of the $2p$ state (solid line), convolution of this profile with the instrument function (dashed line).

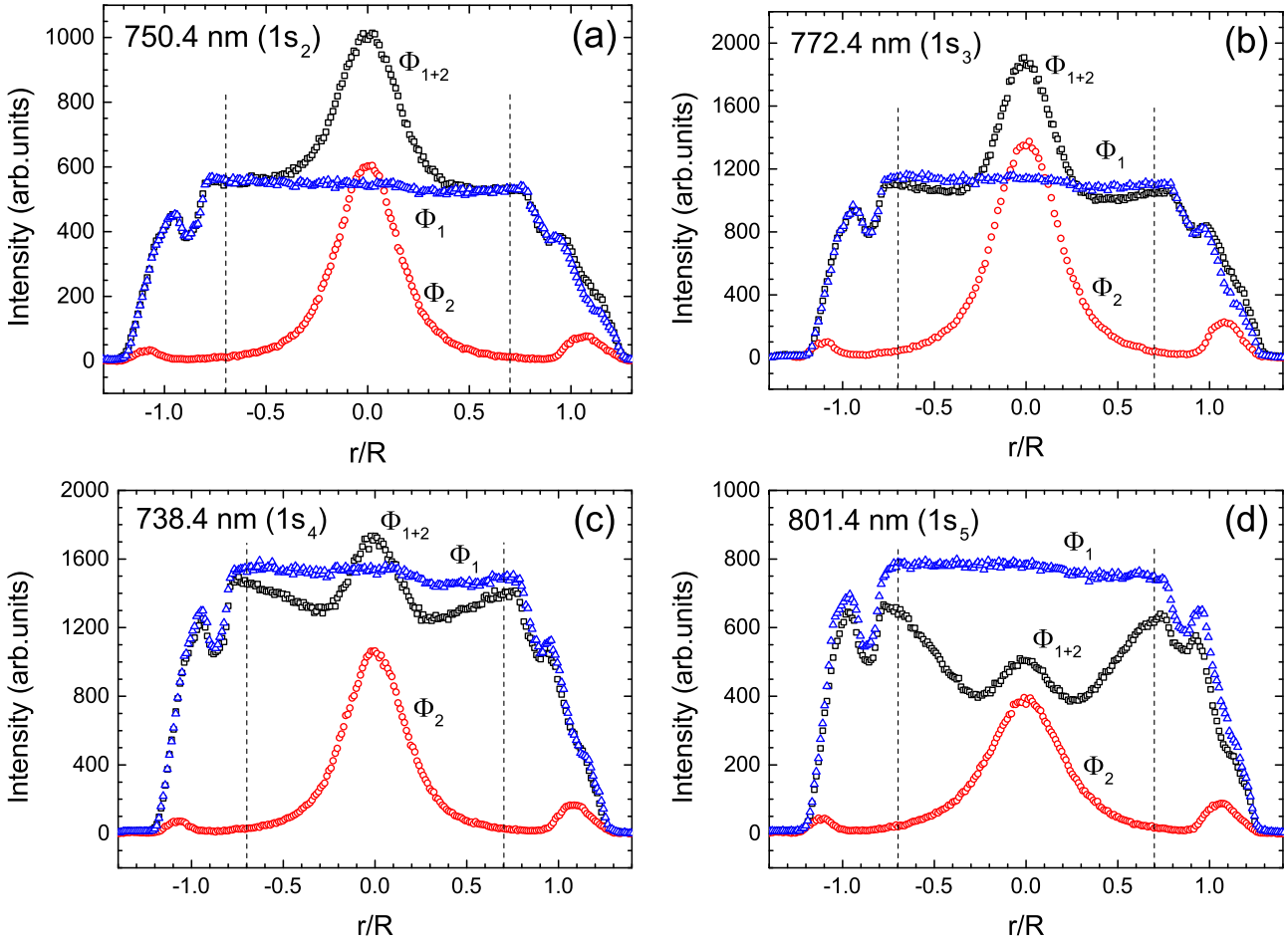

FIG. 5. Examples of spatial profiles of $\Phi_1, \Phi_2, \Phi_{1+2}$ measured in different spectral lines of Ar. Dashed vertical lines determine an area suitable for measurements (excluding the wall reflections).

To obtain the absorption function, one needs to consider line emission and line absorption contours in the present setup. Source Φ_1 is an ICP plasma, a Doppler line shape is assumed for the current discharge configuration, and T_g is estimated as 400 K. For the primary source, a Voigt line shape is assumed. Therefore, expression for the absorption function has the form

$$A(K_0L) = 1 - \frac{1}{\sqrt{\pi}} \int_{-\infty}^{\infty} \exp\left\{ -\omega^2 - \frac{K_0 L}{\varepsilon_0} \times \int_{-\infty}^{\infty} \exp\left[\frac{-x^2}{a^2 + \left(\omega \Delta\nu_1^D/\Delta\nu_2^D - x\right)^2} \right] dx \right\} d\omega,$$

$$\varepsilon_0 = \int_{-\infty}^{\infty} \exp\left(\frac{-x^2}{a^2 + x^2} \right) dx, \quad \omega = \frac{\nu - \nu_0}{\Delta\nu_2^D/2},$$

$$x = \frac{\nu - \nu'}{\Delta\nu_2^D/2}, \quad a = \sqrt{\ln 2}\frac{\Delta\nu_2^D}{\Delta\nu_2^L}. \tag{10}$$

Doppler half-widths and ν_2^L is a Lorentz half width, ν_0 is a center of the spectral line, and a is a Voigt parameter.

For transitions to metastable states, Lorentz half-widths were estimated according to the data from Refs. [51–54]. Resonance broadening was evaluated using the following expression [55,56]:

$$\Delta\lambda = 9.3492 \times 10^{-14} \sqrt{\frac{g_G}{g_R}} \lambda^2 \lambda_R f_R N. \tag{11}$$

Here λ and λ_R are the wavelengths of the observed line and the resonant line, respectively. g_G and g_R are the statistical weights of the ground and resonance states, and f_R is an oscillator strength of the resonance transition. Data on radial distributions of the gas temperature in the glow discharge in argon at tens of Torr were taken from Ref. [15] and correlated with results of the simulation. Due to radial inhomogeneity of the gas temperature, it is necessary to consider radial profiles of the Voigt parameter a to determine the densities of metastable and resonance atoms.

To find radial profiles of the electron density one can measure bremsstrahlung intensity [57]. Figure 6(a) illustrates a measured spectrum of the argon discharge in the region, where the intensity of the continuum reaches a maximum. In the present work, $\lambda = 508.0$ nm was chosen for the measurements. Quantum-mechanical treatment of the bremsstrahlung allows one to relate the intensity of the continuum on the frequency ω with a cross section of electron deceleration, which is averaged

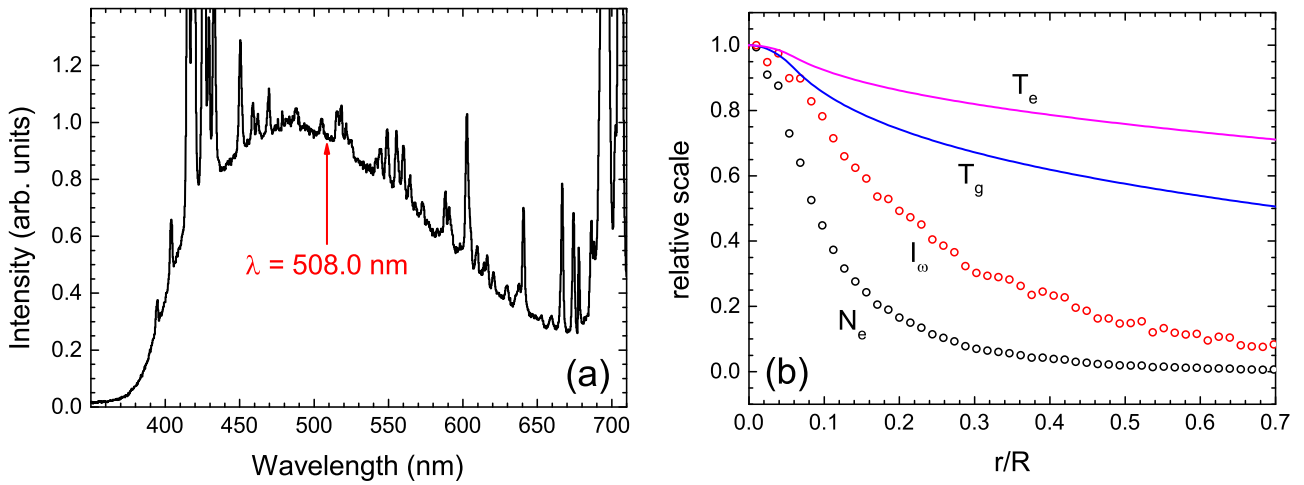

FIG. 6. (a) The measured emission spectrum of the argon glow discharge in the range of intensive continuum. (b) Measured radial profiles of the gas temperature [15], electron temperature, continuum intensity, and electron density.

over distribution function [58,59]:

$$I_\omega = 5\times10^{-3}\frac{N_eN_a}{m^{3/2}c^2}\hbar(kT_e)^{-3/2}\int_{\hbar\omega}^{\infty}\sqrt{\varepsilon-\hbar\omega}\sqrt{\varepsilon}\times[\varepsilon\sigma(\varepsilon-\hbar\omega)-(\varepsilon-\hbar\omega)\sigma(\varepsilon)]e^{-\varepsilon/kT_e}\,d\varepsilon = N_eN_aF(T_e), \quad (12)$$

where the function of the electron temperature is

$$F(T_e) = 5\times10^{-3}\frac{\hbar(kT_e)^{-3/2}}{m^{3/2}c^2}\int_{\hbar\omega}^{\infty}\sqrt{\varepsilon-\hbar\omega}\sqrt{\varepsilon}\times[\varepsilon\sigma(\varepsilon-\hbar\omega)-(\varepsilon-\hbar\omega)\sigma(\varepsilon)]e^{-\varepsilon/kT_e}\,d\varepsilon. \quad (13)$$

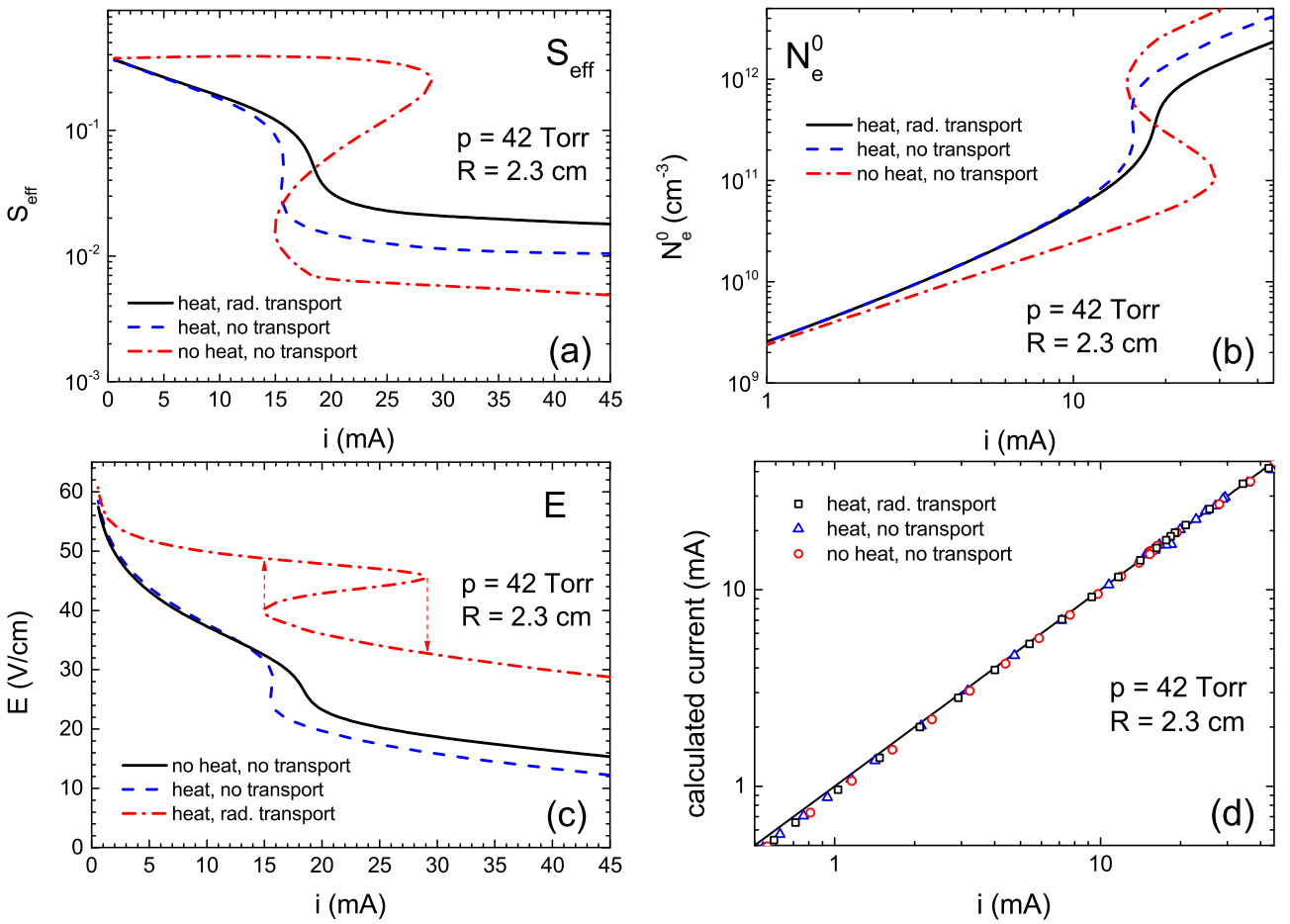

FIG. 7. Discharge characteristics as functions of a current computed in different approximations. (a) The relative current flow area, (b) the axial electron density, (c) the field-current characteristic, (d) test for the identity of expression (15).

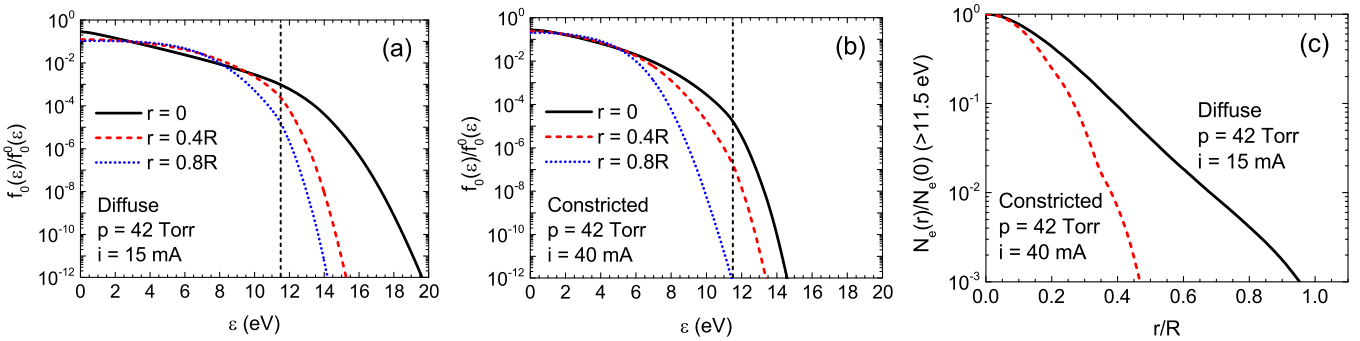

FIG. 8. Electron energy distribution function in case of the (a) diffuse discharge, (b) constricted discharge. The vertical dashed line is the excitation threshold $\varepsilon_{th} = 11.55$ eV. (c) The radial distribution of fast electrons ($\varepsilon > 11.55$ eV).

Here I_ω is a continuum intensity on the frequency ω, $\hbar\omega$ is a corresponding energy of the continuum, σ is a momentum transfer cross section [36], and T_e is the electron temperature.

Equation (12) shows that bremsstrahlung intensity has linear dependence on densities of electrons and neutral atoms. Averaging over Maxwellian EEDF gives dependence on the electron temperature. T_e can be related to the gas temperature by the following approximation: $kT_e \simeq 5.65 \times 10^8 \sqrt{E/N_a} = 5.65 \times 10^8 \sqrt{EkT_g/p}$.

This approximation is derived from the energy balance equation for the case when elastic collisions are dominant. Finally, the electron density can be expressed as $N_e \sim I_\omega [N_a F(T_e)]^{-1} \sim I_\omega T_e^{5/2} \sim I_\omega T_g^{5/4}$, and the radial distribution can be obtained as

$$\frac{N_e(r)}{N_e(0)} \sim \frac{I_\omega(r)}{I_\omega(0)} \left[\frac{T_g(r)}{T_g(0)}\right]^{5/4}. \tag{14}$$

It is worth noting that the thermal inhomogeneity is weak on a scale of the constricted filament in comparison to the electron density [Fig. 6(b)].

The volt-current characteristics were measured by varying the power supply voltage and recorded with a two-channel oscilloscope. The experimental values of the electric field strength were obtained using the relation $E = (U - U_c)/d$, where $U_c \sim 110\ V$ is an estimated value of the cathode voltage drop [14].

IV. RESULTS OF THE SIMULATIONS

A. Validation of the model

In order to test the model the discharge current was calculated using following computed quantities, the relative current flow area $S_{\text{eff}}(i)$ [Fig. 7(a)], the axial electron density $N_e^0(i)$ [Fig. 7(b)] and the weak dependence of an electron mobility b_e on the electric field $E(i)$:

$$i = 2\pi \int_0^R j(r) r\, dr \sim \pi R^2 S_{\text{eff}}(i) N_e^0(i) e b_e E(i),$$
$$S_{\text{eff}} = \frac{2}{R^2} \int_0^R \frac{N_e(r)}{N_e(0)} r\, dr. \tag{15}$$

Substitution of $S_{\text{eff}}(i)$ and $N_e^0(i)$ into expression (15) turns it into the identical relation. Figure 7(d) represents the left and the right sides of expression (15). Although $S_{\text{eff}}(i)$ and $N_e^0(i)$ for the constricted and diffuse regimes differ by orders of magnitude, one can see that the identity relation is valid for the whole considered range of currents. The figure testifies the self-consistency of performed simulations considering

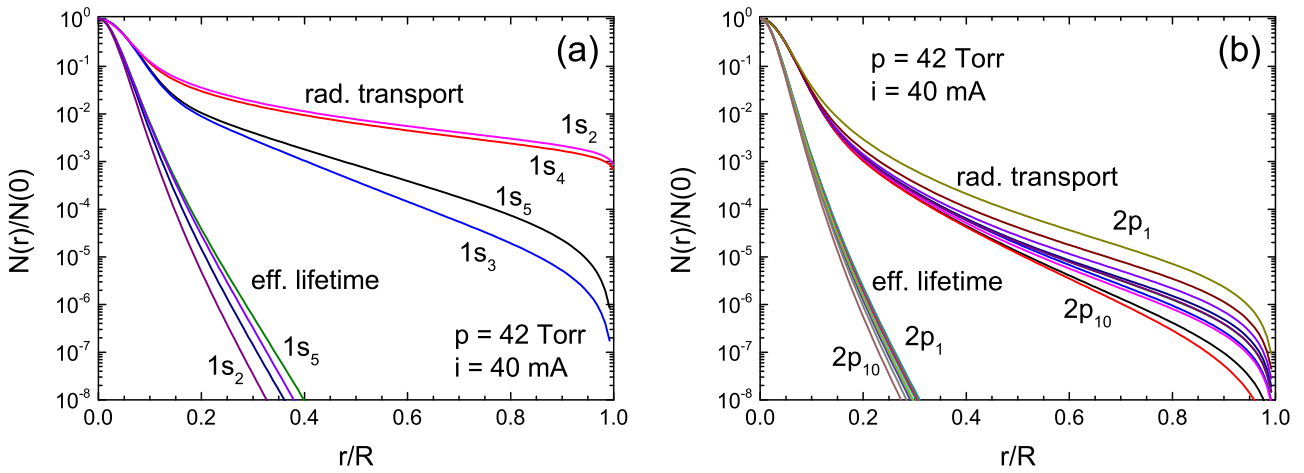

FIG. 9. Influence of the radiation trapping on radial density distributions of the (a) 1$s$states, (b) 2$p$states in the constricted discharge at 40 mA.

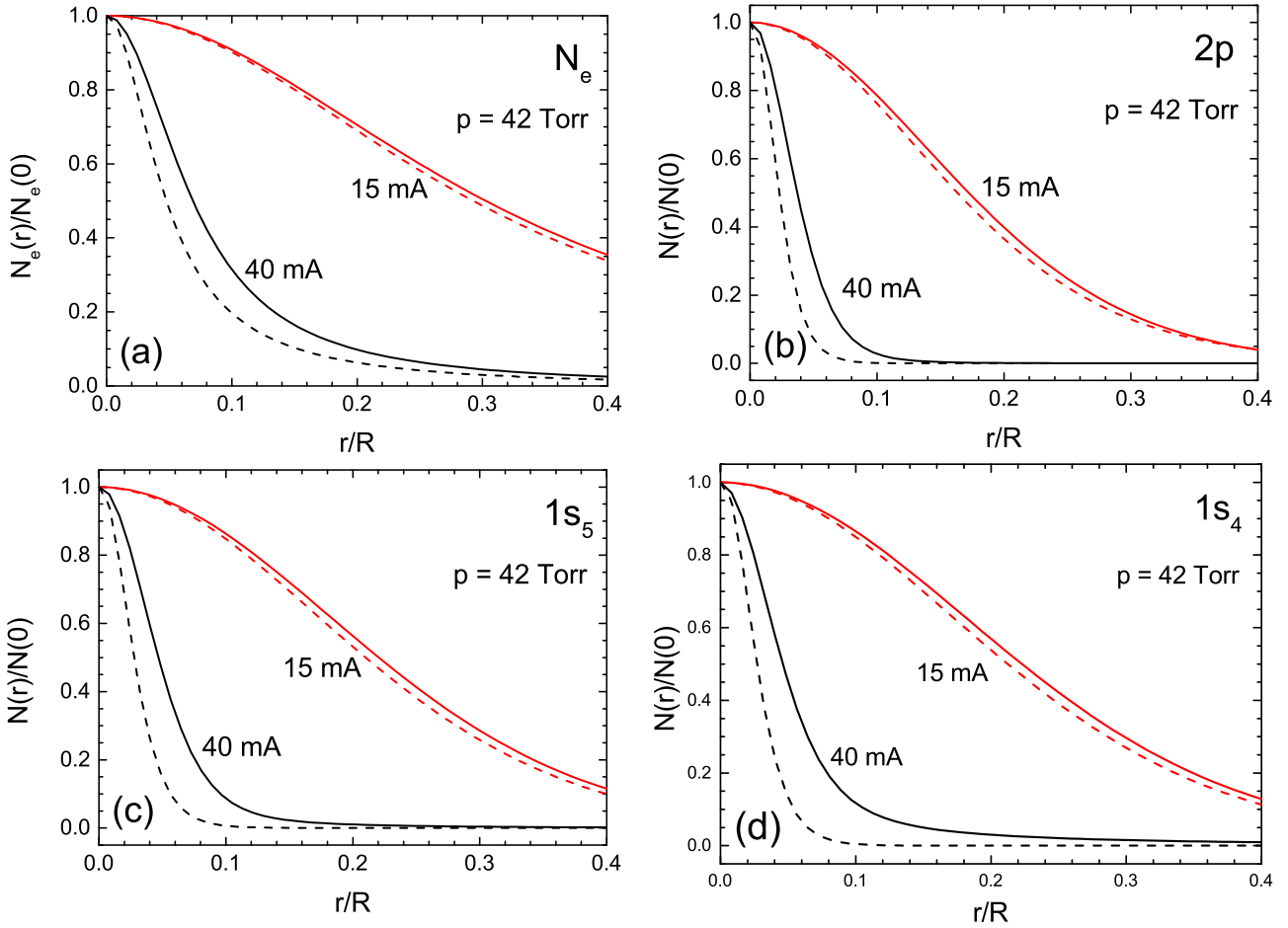

FIG. 10. Influence of the radiation trapping on the density of (a) electrons, (b) $2p$states, (c) metastable atoms in the $1s_5$state, and (d) resonance atoms in the $1s_4$state in Ar at 15 mA (diffuse discharge) and 40 mA (constricted discharge). Dashed lines are profiles, calculated using effective lifetime approximation; solid lines are computed accounting for radiation transport.

different approximations (without the gas heating and the radiation trapping, with the heating neglecting the trapping, and including both the heating and the trapping).

B. EEDF and electrical characteristics

It is interesting to demonstrate the differences in EEDFs for the diffuse and constricted regimes. Figure 8 shows distribution functions in various radial positions for the diffuse discharge at $i = 15$ mA [Fig. 8(a)] and the constricted discharge at $i = 40$ mA [Fig. 8(b)]. Figure 8(c) illustrates the normalized radial distribution of fast electrons, capable for excitation and ionization (with energy > 11.5 eV). One can see that kinetic effects related to the EEDF formation in constricted regime cause dramatic radial losses of fast electrons and contraction of the ionization zone.

Figures 7(a)–7(c) illustrate the discharge characteristics as functions of a current, computed in different approximations. The dash-dotted lines are Z- and S-shaped characteristics with a pronounced hysteresis, obtained without the gas heating and the radiation transport. An account of the gas heating significantly smoothes the curves (dashed lines). Radiation transport slightly shifts those characteristics towards higher currents (solid lines).

C. Influence of the radiation trapping on radial distributions of excited atoms

Simulations with and without the radiation trapping allow one to analyze the changes in radial density profiles of excited

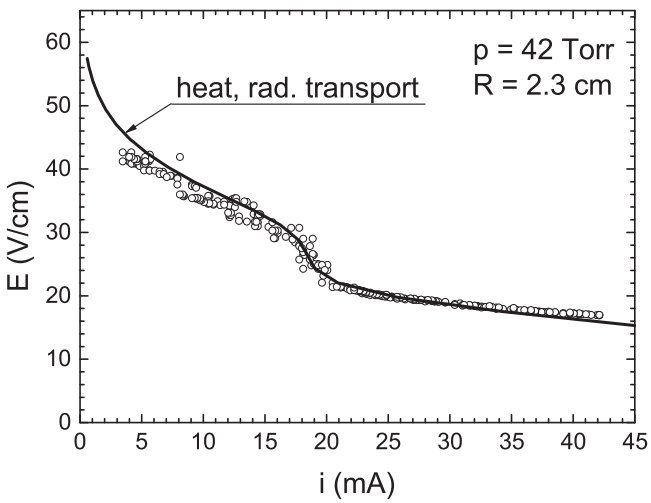

FIG. 11. Field-current characteristic in the Ar discharge at 42 Torr, comparison of the simulation with experimental data.

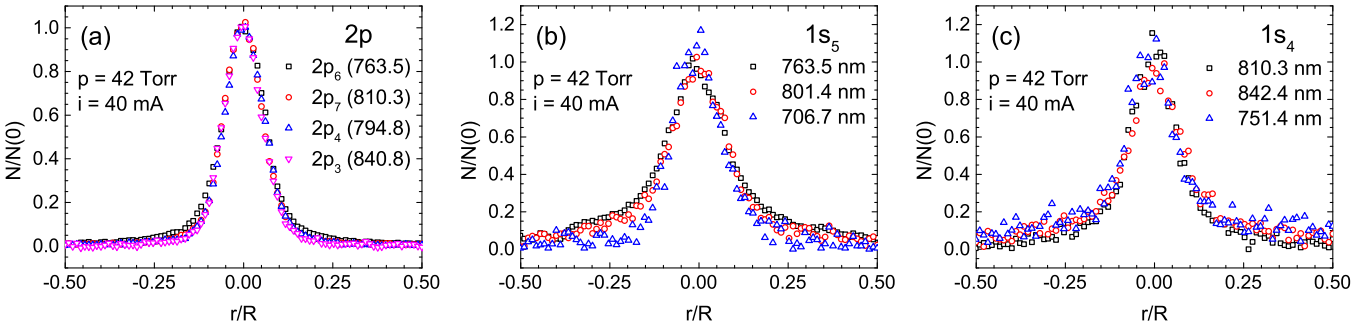

FIG. 12. Radial profiles of excited atoms measured by various spectral lines in constricted Ar discharge at $p = 42$ Torr, $i = 40$ mA: (a) the various $2p$ states, (b) the metastable $1s_5$ state, and (c) the resonance $1s_4$ state.

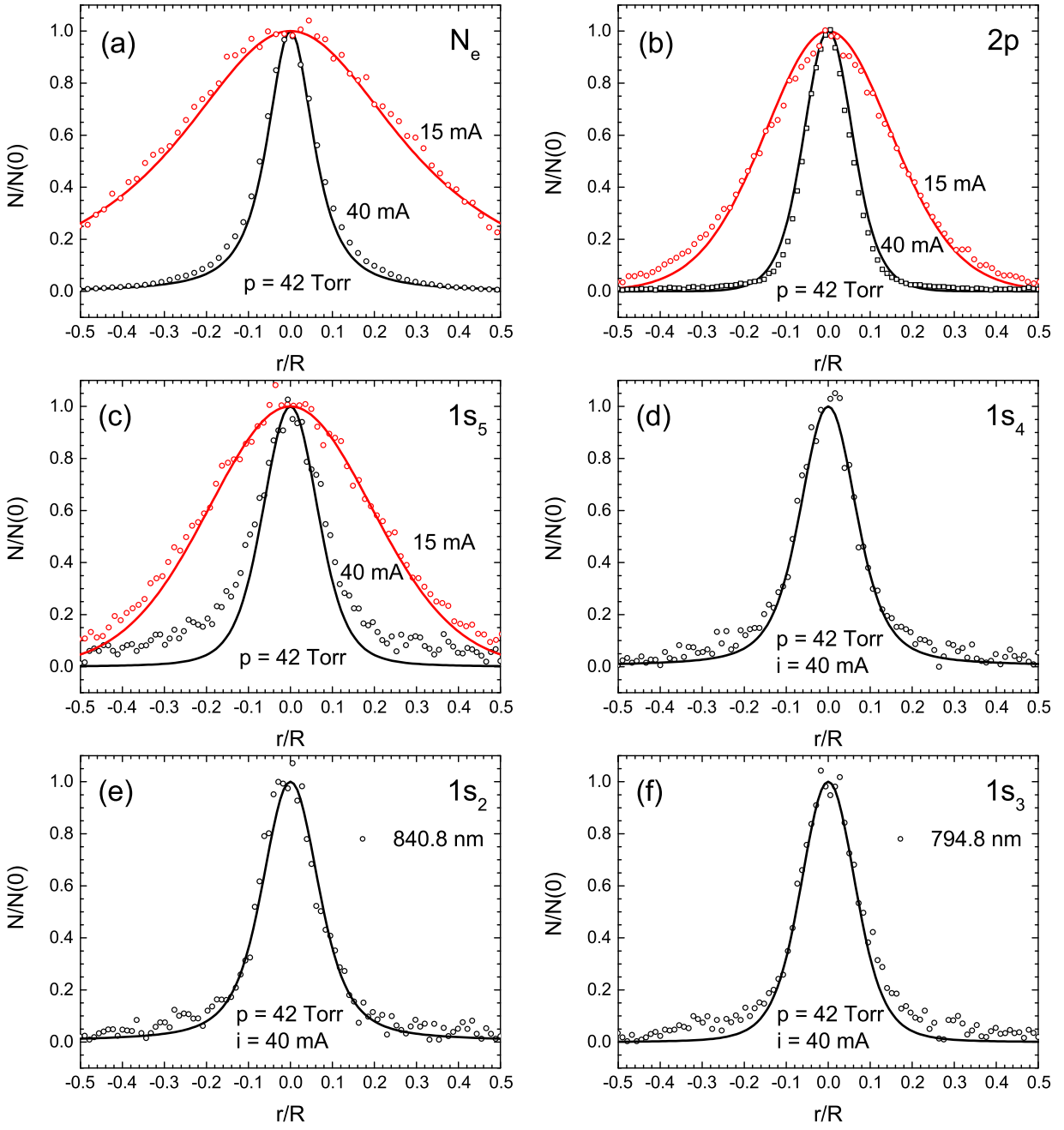

FIG. 13. Measured and calculated radial density profiles at $p = 42$ Torr, $i = 40$ mA. Points, experimental data averaged over lines; lines, convolution of the calculated profile with the instrument function. (a) The electron density, (b) $2p$atoms, (c)–(f) $1s$atoms.

atoms (Fig. 9). Normalized distributions of the metastable ($1s_5$, $1s_3$) and the resonance ($1s_4$, $1s_2$) levels are shown in Fig. 9(a). Figure 9(b) demonstrate profiles of various $2p$ levels. One can see how the radiation transport broadens the radial structure. The effect is most pronounced for the resonance atoms. Metastables and $2p$ atoms are also influenced by the trapping due to the collisional-radiative mixing.

Figure 10 demonstrates how radiation transport affects distributions of excited atoms and electrons in diffuse and constricted discharges. The impact of radiation transport for diffuse discharges is weak. The proximity of the excitation sources to the fundamental eigenmodes of operators of diffusion and radiation transport explains that behavior. The formation of constricted profiles is highly influenced by the higher diffusion (for metastable atoms) and radiation (for resonance atoms) eigenmodes. The mode spectrum, in that case, shows that the amplitude of a fundamental mode is lower than the amplitudes of higher ones. The radiation trapping increases the role of the fundamental mode [60].

D. Comparison with experiment

Figure 11 illustrates the comparison between the computed dependence $E(i)$ and measured data. One can see that results of the simulation with the account for gas heating and radiation trapping agree well with experimental data.

The profiles of different $2p$ levels, corrected for reabsorption, are presented in Fig. 12(a). Despite the fact that modeling predicts some tiny differences between the profiles of different $2p$ levels, they cannot be found experimentally, because they are beyond the spatial resolution limit of the system. Radial profiles of $1s_5$ and $1s_4$ levels, measured in various spectral lines using absorption method, are shown in Figs. 12(b) and 12(c). Those figures illustrate the experimental reproducibility and spatial accuracy of measurements.

The measured and computed radial density profiles of various plasma components are presented in Fig. 13. The diffuse (15 mA lines and points) and the constricted (40 mA lines and points) regimes of the argon positive column are illustrated. Figure 13(a) shows profiles of the electron density. Comparison of the measured and computed distributions of $2p$ atoms is illustrated by Fig. 13(b). The computed values are corrected for experimental instrument distortions (see Sec. III). The experimental densities of metastable and resonance atoms are compared to the theoretical profiles in Figs. 13(c)–13(f). The diffuse regime was investigated only for the lowest level $1s_5$. The populations of other states were not measured because the optical depth in those spectral lines was too small. The comparison shows good agreement between the simulations and the experiment. This good agreement suggests that the proposed theory describes the electric characteristics as well as the formation of narrow filaments and its broadening due to radiation trapping quite well.

V. CONCLUSIONS

A self-consistent model of constriction of the positive column in argon discharge is developed. This model is based on a joint solution of the kinetic equation, which includes elastic and inelastic electron-atomic collisions and electron-electron interaction, balance equations for different species and the thermal conductivity equation. A distinctive feature of the presented model consists of a solution of the Biberman-Holstein equation for resonance atoms on the same accuracy level as for diffusion and thermal conductivity equations. Using the proposed approach one can analyze the influence of resonance radiation transport on various plasma parameters. The theory allows one to obtain not only diffuse and constricted branches of the discharge but also a solution in the unstable region of the hysteresis. It is shown that the diffuse discharge is not affected by radiation transport. In the constricted discharge higher radiative modes play a notable role and cause various changes of discharge parameters. In particular, unstable and constricted branches are shifted to higher currents. Radial profiles of excited states are notably broadened, and axial values are reduced. Resonance radiation trapping affects not only the densities of resonance states $1s_4$, $1s_2$, but also metastable $1s_5, 1s_3$, and higher $2p$atoms due to effective collisional intermixing.

Measurements of VACs, radial density distributions of electrons, and excited states were performed. A good agreement between the results of modeling and the experimental data shows that the proposed theory can accurately describe discharge constriction. This approach discussed in the paper, which includes radiation trapping in a self-consistent model, can be successfully applied to studies of discharges in other gases.

ACKNOWLEDGMENTS

The study was performed with the financial support of the Saint-Petersburg State University (Project No. 11.42.663.2017) and the joint research program "Dmitrii Mendeleev" of DAAD (Project No. 57319844) and the Saint Petersburg State University (Project No. 11.23.818.2017). The work was also supported by a grant of the German-Russian Interdisciplinary Science Center (G-RISC) No. P-2016b-17.

[1] C. Kenty, Phys. Rev. **126**, 1235 (1962).
[2] C. Kenty, J. Chem. Phys. **47**, 2545 (1967).
[3] J. T. Massey and S. M. Cannon, J. Appl. Phys. **36**, 361 (1965).
[4] J. T. Massey, J. Appl. Phys. **36**, 373 (1965).
[5] G. Ecker and O. Zöller, Phys. Fluids **7**, 1996 (1964).
[6] G. Ecker, W. Kröll, and O. Zöller, Phys. Fluids **7**, 2001 (1964).
[7] G. Ecker, W. Kröll, K. H. Spatschek, and O. Zöller, Phys. Fluids **10**, 1037 (1967).
[8] Y. M. Kagan and R. I. Lyagushchenko, Opt. Spectrosc. **17**, 90 (1964).
[9] G. M. Petrov and C. M. Ferreira, Phys. Rev. E **59**, 3571 (1999).
[10] M. Gnybida, D. Loffhagen, and D. Uhrlandt, IEEE Trans. Plasma Sci. **37**, 1208 (2009).

[11] I. A. Shkurenkov, Y. A. Mankelevich, and T. V. Rakhimova, Plasma Phys. Rep. **34**, 780 (2008).
[12] I. A. Shkurenkov, Y. A. Mankelevich, and T. V. Rakhimova, Phys. Rev. E **79**, 046406 (2009).
[13] Y. Z. Ionikh, A. V. Meshchanov, F. B. Petrov, N. A. Dyatko, and A. P. Napartovich, Plasma Phys. Rep. **34**, 867 (2008).
[14] N. A. Dyatko, Y. Z. Ionikh, I. V. Kochetov, D. L. Marinov, A. V. Meshchanov, A. P. Napartovich, F. B. Petrov, and S. A. Starostin, J. Phys. D **41**, 55204 (2008).
[15] Y. B. Golubovskii, S. Gorchakov, D. Loffhagen, A. Timofeev, and D. Uhrlandt, Plasma Sources Sci. Technol. **20**, 55013 (2011).
[16] Z. L. Petrović and A. V. Phelps, Phys. Rev. E **56**, 5920 (1997).
[17] D. Marić, G. Malović, and Z. L. Petrović, Plasma Sources Sci. Technol. **18**, 34009 (2009).
[18] Y. B. Golubovskii, Y. M. Kagan, and R. I. Lyagushchenko, Opt. Spectrosc. **21**, 295 (1966).
[19] T. Holstein, Phys. Rev. **72**, 1212 (1947).
[20] T. Holstein, Phys. Rev. **83**, 1159 (1951).
[21] L. M. Biberman, Zhur. Eksp. i Teoret. Fiz. **17** (1947).
[22] A. V. Phelps, Phys. Rev. **110**, 1362 (1958).
[23] A. V. Phelps and A. O. McCoubrey, Phys. Rev. **118**, 1561 (1960).
[24] A. V. Phelps, Phys. Rev. **117**, 619 (1960).
[25] N. N. Bezuglov, A. K. Kazansky, F. Fuso, and M. Allegrini, Phys. Rev. A **63**, 042703 (2001).
[26] A. K. Kazansky, N. N. Bezuglov, A. F. Molisch, F. Fuso, and M. Allegrini, Phys. Rev. A **64**, 022719 (2001).
[27] J. E. Lawler, G. J. Parker, and W. N. G. Hitchon, J. Quant. Spectrosc. Radiat. Transfer **49**, 627 (1993).
[28] G. J. Parker, W. N. G. Hitchon, and J. E. Lawler, J. Phys. B **26**, 4643 (1993).
[29] N. R. Pinhão, J. Phys. D **27**, 1184 (1994).
[30] H. J. Lee and J. P. Verboncoeur, Phys. Plasmas **9**, 4804 (2002).
[31] J. Giuliani, G. Petrov, J. P. Apruzese, and J. Davis, Plasma Sources Sci. Technol. **14**, 236 (2005).
[32] Y. B. Golubovskii, I. A. Porokhova, H. Lange, and D. Uhrlandt, Plasma Sources Sci. Technol. **14**, 36 (2004).
[33] Y. B. Golubovskii and V. A. Maiorov, Plasma Sources Sci. Technol. **24**, 25027 (2015).
[34] J. A. Hornbeck, Phys. Rev. **84**, 615 (1951).
[35] S. Neeser, T. Kunz, and H. Langhoff, J. Phys. D **30**, 1489 (1997).
[36] M. Hayashi, Bibliography of electron and photon cross sections with atoms and molecules published in the 20th century. Argon, Tech. Rep. (National Inst. for Fusion Science, 2003), https://inis.iaea.org/search/search.aspx?orig_q=RN:34071469.
[37] C. M. Ferreira, J. Loureiro, and A. Ricard, J. Appl. Phys. **57**, 82 (1985).
[38] V. M. Donnelly, J. Phys. D **37**, R217 (2004).
[39] W.-C. F. Liu and D. C. Conway, J. Chem. Phys. **62**, 3070 (1975).
[40] Y.-J. Shiu and M. A. Biondi, Phys. Rev. A **17**, 868 (1978).
[41] V. S. Marchenko, Zh. Eksp. Teor. Fiz **85**, 510 (1983) [Sov. Phys. JETP **58**, 292 (1984)].
[42] A. Kramida, Y. Ralchenko, and J. Reader, J. Res. Natl. Inst. Stand. Technol. (2013), https://www.nist.gov/pml/atomic-spectra-database.
[43] P. Millet, A. Birot, H. Brunet, H. Dijolis, J. Galy, and Y. Salamero, J. Phys. B **15**, 2935 (1982).
[44] J. W. Keto, R. E. Gleason, T. D. Bonifield, G. K. Walters, and F. K. Soley, Chem. Phys. Lett. **42**, 125 (1976).
[45] K. Tachibana, Phys. Rev. A **34**, 1007 (1986).
[46] S. Pfau, A. Rutscher, and K. Wojaczek, Contrib. Plasma Phys. **9**, 333 (1969).
[47] D. Loffhagen, Plasma Chem. Plasma Process. **25**, 519 (2005).
[48] Y. B. Golubovskii, V. O. Nekuchaev, and A. V. Siasko, Russ. J. Phys. Chem. B **9**, 533 (2015).
[49] Y. B. Golubovskii, D. Kalanov, S. Gorchakov, and D. Uhrlandt, Plasma Sources Sci. Technol. **24**, 025028 (2015).
[50] R. Ladenburg and S. Levy, Z. Phys. **65**, 189 (1930).
[51] G. H. Copley and D. M. Camm, J. Quant. Spectrosc. Radiat. Transfer **14**, 899 (1974).
[52] D. P. Aeschliman, R. A. Hill, and D. L. Evans, Phys. Rev. A **14**, 1421 (1976).
[53] O. Vallee, P. Ranson, and J. Chapelle, J. Quant. Spectrosc. Radiat. Transfer **18**, 327 (1977).
[54] K. Tachibana, H. Harima, and Y. Urano, J. Phys. B **15**, 3169 (1982).
[55] E. L. Lewis, Phys. Rep. **58**, 1 (1980).
[56] A. V. Pipa, Y. Z. Ionikh, V. M. Chekishev, M. Dunnbier, and S. Reuter, Appl. Phys. Lett. **106**, 244104 (2015).
[57] A. Rutscher and S. Pfau, Physica B+C **81**, 395 (1976).
[58] V. Kas'yanov and A. Starostin, Sov. Phys. JETP **21**, 193 (1965).
[59] C. Yamabe, S. J. Buckman, and A. V. Phelps, Phys. Rev. A **27**, 1345 (1983).
[60] Y. B. Golubovskii, A. V. Siasko, and V. O. Nekuchaev, Plasma Sources Sci. Technol. **26**, 15012 (2016).